Supplement of Atmos. Chem. Phys., 26, 12037–12047, 2026
https://doi.org/10.5194/acp-26-12037-2026-supplement

Atmospheric Chemistry and Physics
Open Access

Supplement of

Buffering of atmospheric nanoparticle growth by temperature-dependent shifts in molecular composition, volatility and diffusivity

Zhiqiang Zhang et al.

Correspondence to: Thomas Berkemeier (t.berkemeier@mpic.de)

Supplementary Text

S1 Kinetic multilayer model of multiphase chemistry

We use the kinetic multilayer model of multiphase chemistry (KM3C) to explicitly treat gas phase diffusion, particle-phase bulk diffusion, and multiphase partitioning kinetics based on vapor pressures (Fig. S9). KM3C is built in the framework of the kinetic multilayer meta model (KM-MEMO, Mishra et al., 2025), which is a Matlab toolkit that simplifies kinetic model construction by automatically generating and executing systems of differential equations from well-defined input files. KM3C addresses possible limitations in surface-bulk mass transfer and bulk diffusion, and detailed descriptions of the model and its predecessors are described elsewhere (Shiraiwa et al., 2012; Berkemeier et al., 2020; Kang et al., 2026). The model consists of the following compartments: gas phase, near-surface gas phase, a sorption layer, a quasi-static surface layer (near-surface bulk layer), and the particle bulk, subdivided into several bulk layers. The model is initiated with a freshly-nucleated particle (diameter of 0.9 nm) containing non-volatile organic species. When modeling the CERN CLOUD laboratory data, we fix the concentrations of gaseous OOMs to the values reported in Stolzenburg et al. (2018). When modeling the field measurement data, we interpolate the concentrations reported in Stolzenburg et al. (2025) of gaseous OOMs and H_2SO_4 across several time intervals.

In this study, we use a volatility basis set (VBS) approach that categorizes molecules by their saturation mass concentrations at 298 K (C^*_{298}) into logarithmically spaced volatility bins (Donahue et al., 2006, 2014; Stolzenburg et al., 2022). KM3C treats each volatility bin as a representative chemical species. For the field measurement data, we use average molecular weights reported for each volatility bin. For the CERN CLOUD chamber data, we use a linear relationship of volatility and molecular weight that we derive from the field measurements in a molecular corridor plot (Table S1 and Fig. S10, Shiraiwa et al., 2014). The model corrects C^*_{298} for temperature with the Clausius-Clapeyron equation (Eq. S1) and the enthalpy of vaporization (ΔH_{vap}), where R is the gas constant. We calculate the ΔH_{vap} for each volatility bin using the empirical relationship between C^*_{298} and ΔH_{vap} (Eq. S2) proposed by Epstein et al. (2010) and use the parameters from Stolzenburg et al. (2022). An upper limit of 200 kJ mol^{-1} is applied to ΔH_{vap} (Cappa and Jimenez, 2010).

$$C^*(T) = C^*_{298} \times \exp\left(-\frac{\Delta H_{\text{vap}}}{R}\left(\frac{1}{T} - \frac{1}{298}\right)\right) \tag{S1}$$

$$\Delta H_{\text{vap}} = -5.7 \times \log_{10}(C^*_{298}) + 129 \tag{S2}$$

KM3C is sensitive to the bulk diffusion coefficient, which we vary across the range characteristic for liquid to solid phases. Nanoparticle growth is affected by lowered diffusivities in two ways: development of differential concentration gradients (i.e. different compounds exhibit concentration gradients of different strength and direction) and reduced surface-to-bulk transfer. Both lead to reduced condensation of relatively higher volatile compounds (SVOC, LVOC).

The model describes the temperature-dependence of bulk diffusivity with a similar Arrhenius-type equation (Eq. S3) and an activation energy of diffusion ($E_{\mathrm{a,dif}}$). Here, we use a value of $E_{\mathrm{a,dif}}$ = 40 kJ mol^{-1}, which is consistent with that of sucrose-water solutions (Kiland et al., 2019).

$$D_b(T) = D_{\mathrm{b,298}} \times \exp\left(-\frac{E_{\mathrm{a,dif}}}{R}\left(\frac{1}{T} - \frac{1}{298}\right)\right) \tag{S3}$$

We note that $E_{\mathrm{a,dif}}$ will likely increase towards more viscous organic matrices, leading to super-Arrhenius behavior when approaching the glass transition, a property well-known from studies of the viscosity of so-called fragile glass-formers (Angell, 1991). Diffusion coefficients used in this study at different temperatures for simulating nanoparticle growth in field and CERN CLOUD chamber studies are listed in Table S2. A more detailed description of the composition- and temperature-dependence of the diffusion coefficient in organic nanoparticle growth can be found in Sects. S7 and S8 below.

Another process affecting nanoparticle growth is coagulation, which can increase measured growth rates (Cai et al., 2021, 2026). Coagulation was not explicitly treated in this study, as Stolzenburg et al. (2025) reported little influence of coagulation for the investigated field data, while Stolzenburg et al. (2018) included it into their uncertainty estimates for the investigated chamber data. Following Nguyen et al. (2026), we estimated the self-coagulation timescale (τ_{scoa}, Eq. S4) and show the results in Fig. S11.

$$\tau_{\mathrm{scoa}} = \frac{2}{K N_{\mathrm{p}}} \tag{S4}$$

where, N_{p} is the particle number concentration and K is the coagulation coefficient. We derive K from the formulas given in Nguyen et al. (2026) as a function of particle diameter, Brownian diffusivity, mean thermal velocity, and coagulation efficiency (α). For details on the calculation of K, please refer to Table S1 in Nguyen et al. (2026). At a particle number concentration of 10^3 cm^{-3} (Stolzenburg et al., 2025), characteristic self-coagulation timescales (star-shaped markers) are much longer than the observation time of 6 hours (gray dashed line), irrespective of particle size (shadings) and coagulation efficiency (blue vs. black lines). Previous studies also suggested viscous particles might adopt a lower coagulation efficiency (Hou et al., 2020), which would further prolong the coagulation timescale. Besides self-coagulation, scavenging of nanoparticles by larger particles may occur, but these particles then simply do not contribute to nanoparticle growth rates measured by the appearance time method. Therefore, we assume a negligible impact of coagulation in this study. Moreover, the analysis and description of nanoparticle growth rates in atmospheric air masses can be influenced by differences between Lagrangian and Eulerian perspectives in the analysis and modeling of condensable vapor concentrations and aerosol particle size distributions. Such effects were not taken into account here but will be investigated in follow-up studies combining KM3C with regional and global 3D models of atmospheric transport and chemistry.

S2 Mass transfer coefficients

In KM3C, diffusion limitations affect growth rates mostly by slowing surface-to-bulk transfer, i.e. the transition of a molecule between being surface-adsorbed and being absorbed into the particle bulk. The surface-to-bulk transfer rate is directly proportional to the diffusivity in the topmost bulk layer and inversely proportional to the vapor pressure of the transported molecule (Shiraiwa et al., 2012; Berkemeier et al., 2020). Based on absorptive partitioning theory (Pankow, 1994), the surface-to-bulk transfer rate coefficient (k_{sb}) is calculated with Eq. S5:

$$k_{\mathrm{sb}} = \frac{2D_{\mathrm{b}}}{\delta_{\mathrm{s}} + \delta_{\mathrm{b1}}} \frac{k_{\mathrm{d}}}{k_{\mathrm{a}}} \frac{\sum [Y_i]_{\mathrm{b1}} RT}{p_{\mathrm{vap}} N_{\mathrm{A}}} \tag{S5}$$

in which, k_{d} and k_{a} are the desorption and adsorption rate coefficients. $\sum [Y]_{\mathrm{b1}}$ is the sum of the molecular concentrations of all species Y_i in the near-surface bulk layer. p_{vap} is the vapor pressure of the partitioning species, R is the gas constant, T is the temperature, and N_{A} is Avogadro's number. k_{bs} is the bulk-to-surface transfer rate coefficient and is calculated with Eq. S6, where D_{b} is the bulk diffusivity, δ_{s} is the depth of sorption layer, and δ_{b1} is the depth of the near-surface bulk layer.

$$k_{\mathrm{bs}} = \frac{2D_{\mathrm{b}}}{\delta_{\mathrm{s}} + \delta_{\mathrm{b1}}} \tag{S6}$$

We use a first-order adsorption rate coefficient (k_{a}, Eq. S7), where α and ω are the mass accommodation coefficient and the mean thermal velocity of the adsorbing molecule respectively. C_{g} and θ are the gas phase diffusion correction factor and the fractional surface coverage (Shiraiwa et al., 2012).

$$k_{\mathrm{a}} = C_{\mathrm{g}} \alpha \frac{\omega}{4} (1 - \theta) \tag{S7}$$

To obtain the total flow of adsorption F_{ads} (unit s^{-1}) of molecules to the particle surface, k_{a} is multiplied with the near-surface gas concentration [$\mathrm{Z_{gs}}$] and the collision cross section A_{p} of the particle (Pöschl et al., 2007). This effective collision surface area of the particle in KM3C is calculated using the particle radius plus the sorption layer, for which we assume a thickness of 0.639 nm, corresponding to organic matter with an average molar mass of 220 g mol^{-1} and density of 1.4 g cm^{-3}.

The first-order desorption rate coefficient (k_{d}, Eq. S8) is the inverse of the surface desorption lifetime (τ_{d}), where A_{des} is the pre-exponential factor ($A_{\mathrm{des}} = 10^{13}$) and E_{des} is the activation energy of desorption (Knopf et al., 2024). Using literature values, Knopf et al. (2024) found a relationship between the standard saturation vapor pressure $p_{\mathrm{vap,298}}$ and E_{des}, which is shown in Fig. S12 and depends on the molecular oxygen-to-carbon ratio (O:C). As the organic compounds condensing on nanoparticles are likely highly oxygenated, we use a parameterization that runs along the left boundary of the data in this study. Note, however, that the choice of τ_{d} was not sensitive in the model simulations unless much larger values were chosen.

$$k_{\mathrm{d}} = \frac{1}{\tau_{\mathrm{d}}} = A_{\mathrm{des}} \exp\left(\frac{-E_{\mathrm{des}}}{RT}\right) \tag{S8}$$

The model corrects the vapor pressures for the Kelvin effect (Seinfeld and Pandis, 2016) by multiplying the vapor pressures with the Kelvin term ($K(D_\mathrm{p})$, Eq. S9). Here, D_p is the diameter of the particle, and D_{K10} is the Kelvin diameter at which the curvature effect becomes important (Eq. S10).

$$K(D_\mathrm{p}) = 10^{(D_{K10}/D_\mathrm{p})} \tag{S9}$$

$$D_{K10}(T) = 4.8 \times (300 \times T^{-1}) \tag{S10}$$

In line with the results by Tröstl et al. (2016), we find the impact of the Kelvin term on the simulation results to be rather small.

S3 Adaptive layer resizing algorithm

KM3C adopts an adaptive layer resizing algorithm that dynamically splits layers when a layer grows too large and merges adjacent layers when they are too thin (Kang et al., 2026). This algorithm is able to account for concentration gradients dynamically as particles grow (or shrink) and can prevent numerical stiffness that arises when layers deplete. As the particles grow, solvating molecules enter the near-surface bulk layer, which can trigger a split of that layer via the adaptive layer resizing algorithm. However, this split can lead to an artificial and sudden increase in particle growth as k_sb and k_bs increase when δ_b1 decreases. To solve this problem, we implement a moving-boundary algorithm (Couvidat and Sartelet, 2015; Kang et al., 2026), which keeps the depth of the near-surface bulk layer constant by increasing mass transport from the near-surface bulk layer to the underlying bulk layer when the the near-surface bulk layer grows. The enhanced diffusion is calculated based on the molecular volume flow into the near-surface bulk layer. The near-surface bulk layer in KM3C adopts the role and properties of the quasi-static surface layer formalized and used in previous studies (Pöschl et al., 2007; Shiraiwa et al., 2012).

S4 Hyytiälä SMEAR II station field measurement data

Stolzenburg et al. (2025) reported field measurements of H_2SO_4, OOMs and nanoparticle growth at the SMEAR II station in the boreal forests of Hyytiälä, Finland from April 11th (3.8 °C, 50.7 % RH) and August 17th (17.5 °C, 49.9 % RH) of 2020 (Gonzalez Carracedo et al., 2022). The brown line and shadings in Fig. 1 in the main text shows the best estimate and uncertainty range of traditional model calculations. Shadings are obtained by shifting the volatility basis set by ± 1 bin. We use the same methodology for the uncertainty range of the KM3C model calculations. The authors also reported OOMs volatility distributions estimated using the identified molecular ion signals and a parameterization based on elemental ratios (Donahue et al., 2011). We use the reported ion masses for the molecular weights of the volatility bin species in KM3C (black and blue markers in Fig. S10).

S5 CERN CLOUD laboratory data

We use laboratory experimental data of dark α-pinene ozonolysis conducted at the Cosmics Leaving Outdoor Droplets (CLOUD) chamber at the European Organization for Nuclear Research (CERN) (Kirkby et al., 2011; Stolzenburg et al., 2018). Experiments were performed at three different temperatures (25, 5, and -25 °C). Proton transfer reaction (PTR3) and nitrate chemical ionization mass spectrometers (NO3-CIMS) were used to measure the gas-phase species. Stolzenburg et al. (2018) reported detailed organic vapor concentrations and volatility distributions for three experiments, which we digitized from the published Fig. 1 using WebPlotDigitizer. We simulate the experiments with KM3C at the temperatures reported and assuming $D_{\mathrm{b},298}$ = 10^{-18} cm^2 s^{-1}. The simulation results are displayed as square markers in Fig. 3 in the main text. Stolzenburg et al. (2018) did not report the specific ion masses, and we estimate the molecular weights for the products in the CLOUD experiments using the ion masses in Stolzenburg et al. (2025) (Table S1). These values are shown as the red circles in Figure S10. Colored bands in Fig. 2 in the main text are obtained by linearly scaling the condensable organic vapor concentrations in the model at the three respective temperatures (-25, 5, and 25°C) to obtain a series of model simulations at the same temperatures. In main text Fig. 2, we vary the bulk diffusion coefficient within the semi-solid phase state range (10^{-20} – 10^{-15} cm^2 s^{-1}) and scale with temperature to obtain the upper and lower boundaries of the colored bands.

The growth rates observed at high temperature in the CERN CLOUD chamber experiments of α-pinene ozonolysis under dark conditions (25°C, yellow bands and data points) are best reproduced assuming relatively low diffusivity for particles smaller than 3 nm (Fig. 2a in the main text) and higher diffusivity for larger nanoparticles (Fig. 2b in the main text). In contrast, reproducing the boreal summertime field observations requires low diffusivity for the entire size range up to 11 nm (Fig. 1a in the main text). These differences in diffusivity can be plausibly attributed to differences in particle composition and chemical aging. As shown in Fig. S2, smaller particles contain higher proportions of organic compounds with low intrinsic volatility (ELVOC/ULVOC), while the uptake and partitioning of relatively more volatile compounds (SVOC/LVOC) tend to reduce the viscosity and increase the diffusivity of larger particles. Intrinsic volatility is often characterized by the saturation mass concentration at a standard temperature of 298 K (C^*_{298}, Schervish and Donahue, 2020; Donahue et al., 2026).

The molecular composition of SOA particles formed by dark ozonolysis of α-pinene (CERN CLOUD) is likely not the same as for particles formed in summertime boreal forest air (Hyytiälä), which may be influenced by other volatile precursors (monoterpenes, sesquiterpenes; Hellén et al., 2018) and photo-oxidants including OH radicals. Furthermore, sunlight and atmospheric photochemistry may promote condensed-phase reactions that can enhance the formation of more highly oxygenated compounds, dimers, oligomers, and other accretion products. Such condensed-phase reaction products with high molecular mass and low volatility can influence particle composition, viscosity, and diffusivity without being reflected in gas-phase measurements of condensable organic vapor concentrations and volatility distributions (Mehra et al., 2020; Maben and Ziemann, 2023; Kenseth et al., 2023; Kang et al., 2026). An accurate description of SOA nanoparticle growth may thus require resolution of molecular identities, their chemical evolution along molecular corridors, as well as matrix interactions influencing their physicochemical properties (Sect. S10; Shiraiwa et al., 2014; Li et al., 2016; Knopf et al., 2024).

To obtain shaded regions in main text Fig. 3, we scale the obtained growth rates by a factor of 3 to account for experimental uncertainties, possible differences in the ambient vapor composition compared to the CERN CLOUD measurements, and possible differences in particle phase state.

S6 Determination of nanoparticle growth rates

In both, KM3C used in this study and the two-film model used in Stolzenburg et al. (2025), the diameter growth rate of the particle (GR = $\mathrm{d}d_p/\mathrm{d}t$) was calculated from the $d_p(t)$ trajectory of a monodisperse particle population. The growth rate within a size interval is determined from the time required for a monodisperse particle to grow from one end of the size interval to the other:

$$GR_{1.5\text{–}3\,\mathrm{nm}} = \frac{\Delta d_p}{\Delta t_{1.5\text{–}3\,\mathrm{nm}}} = \frac{1.5\,\mathrm{nm}}{\Delta t_{1.5\text{–}3\,\mathrm{nm}}} \tag{S11}$$

$$GR_{3\text{–}7\,\mathrm{nm}} = \frac{\Delta d_p}{\Delta t_{3\text{–}7\,\mathrm{nm}}} = \frac{4\,\mathrm{nm}}{\Delta t_{3\text{–}7\,\mathrm{nm}}} \tag{S12}$$

For the CLOUD experiment, growth rate was estimated by the appearance-time method in the original study (Stolzenburg et al., 2018). In the Hyytiälä field measurements, growth rates were estimated with the appearance-time and maximum-concentration methods (Stolzenburg et al., 2023). Specifically, the maximum concentration method defines the representative time (t) as when the particle number concentration within a specific size bin peaks (Kulmala et al., 2013), typically determined by fitting a Gaussian function to each size channel's signal. The resulting time shift as a function of particle size reflects particle growth. The appearance time method uses the time (t_m) when the concentration reaches a specific percentage ($m\%$) of its maximum during an new particle formation event (Lehtipalo et al., 2014).

S7 Temperature-dependent diffusivity coefficients

The diffusivity in organic matter condensing at high temperature may be lower than in organic matter condensing at low temperature. For a certain gas-phase composition, this depends on the magnitudes of the enthalpies of vaporization and the activation energies of diffusion (Epstein et al., 2010; Kiland et al., 2019). The volatilities of organic compounds show Arrhenius-behavior following the Clausius-Clapeyron equation, but the viscosity of organic liquids approaching the glass transition generally exhibits super-Arrhenius behavior following the Vogel–Fulcher–Tammann equation (Bilde et al., 2015; Shiraiwa et al., 2017), which means that activation energies of diffusion are not constant over large temperature ranges. This interplay is important for determining whether a multiphase system of condensing vapors exhibits hardening or softening of the particle phase upon increase in temperature. In semi-solids, activation energies of diffusion may be smaller than enthalpies of vaporization, which would entail a hardening of organic aerosols towards higher temperatures. For glassy organics, however, activation energies

of diffusion may be larger than enthalpies of vaporization and the dependence may reverse: a liquefaction of organic aerosols towards higher temperatures.

S8 Composition-dependent diffusivity coefficients

The diffusivity of a mixture of organic molecules depends on its chemical composition. We explore the implementation of parameterizations of bulk diffusivity (D_b) as function of saturation mass concentration (C^*) of different volatility bins. In the following, we present parameterizations developed by Li et al. (2020) (Sect. S8.1) and Kang et al. (2026) (Sect. S8.4). Afterwards, we explore the effects of plasticization by water (Sect. S8.2) and the size-dependence of aerosol phase state as suggested by Cheng et al. (2015) and investigated by Mahant et al. (2024) (Sect. S8.3).

S8.1 T_g-C^* parameterization by Li et al. (2020)

We calculate the glass transition temperature (T_g) of individual species i based on the parameterization proposed by Li et al. (2020):

$$T_{g,i} = 288.70 - 15.33 \times \log_{10}(C^*_{298}) - 0.33 \times \log_{10}(C^*_{298}) \tag{S13}$$

The glass transition temperature of the mixture within layer l is calculated from the $T_{\mathrm{g},i}$ of the individual species, weighted with their mass fraction ($w_{i,l}$) in that layer.

$$T_{\mathrm{g},l} = \sum_i w_{i,l} T_{\mathrm{g},i} \tag{S14}$$

As the T_g of sulfate, we assume the value measured by ammonium bisulfate of 220 K (Dette and Koop, 2015). The viscosity (η_l) of mixture in layer l can be calculated from the average $T_{\mathrm{g},l}$ with the Vogel–Fulcher–Tammann (VFT) equation.

$$T_{0,l} = \frac{39.17 \times T_{\mathrm{g},l}}{D + 39.17} \tag{S15}$$

$$\eta_l = \eta_\infty e^{\frac{T_{0,l} D}{T - T_{0,l}}} \tag{S16}$$

where η_∞ is the viscosity at infinite temperature (10^{-5} Pa s; Angell (1991)). $T_{0,l}$ is the Vogel temperature, which was derived assuming η_l = 10^{12} Pa s when T = $T_{\mathrm{g},l}$. For T < $T_{\mathrm{g},l}$, η_l is capped at 10^{12} Pa s. D is the fragility parameter, which is assumed to be 10 here. T is the temperature.

From the glass transition temperature and viscosity of the mixture, we calculate molecular diffusivities in layer l based on the Stokes-Einstein relation (Koop et al., 2011).

$$D_{\mathrm{b},l} = \frac{kT}{6\pi r_l \eta_l} \tag{S17}$$

Here, k is the Boltzmann constant. r_l is the radius of the diffusing species in layer l, which is the average effective molecular length of all species.

S8.2 Plasticization of water as a function of relative humidity

T_{g} of organics (H_2SO_4)-water mixtures at given RH can be estimated using the Gordon-Taylor equation (Gordon and Taylor, 1952).

$$T_{\mathrm{g},l}(w_{\mathrm{org},l}) = \frac{(1-w_{\mathrm{org},l})T_{g,\mathrm{w}} + \frac{1}{k_{\mathrm{GT}}} w_{\mathrm{org},l} T_{\mathrm{g},l}}{(1-w_{\mathrm{org},l}) + \frac{1}{k_{\mathrm{GT}}} w_{\mathrm{org},l}} \tag{S18}$$

where $w_{\mathrm{org},l}$ is the mass fraction of organics and H_2SO_4 in layer l. $T_{g,\mathrm{w}}$ is the glass transition temperature of water (136 K). k_{GT} is the Gordon-Taylor constant (2.5). We calculate the mass fraction of water with Raoult's law and the effective hygroscopicity parameter (κ; Petters and Kreidenweis (2007)), and then $T_{\mathrm{g},l}(w_{\mathrm{org},l})$ of organics (H_2SO_4)-water mixtures in layer l is used in Eq. S15 and the following calculations.

In the effective hygroscopicity parameter method, the mass concentrations of water absorbed by nanoparticles can be estimated as:

$$m_{\mathrm{H_2O},l} = \frac{\kappa \rho_{\mathrm{w}} m_{\mathrm{SOA},l}}{\rho_{\mathrm{SOA}} \left(\frac{1}{a_{\mathrm{w}}} - 1\right)} \tag{S19}$$

where ρ_{w} and ρ_{SOA} are the densities of water (1 g cm^{-3}) and organics (1.4 g cm^{-3}), respectively. $m_{\mathrm{SOA},l}$ is the mass concentration of organics in layer l. a_{w} is the water activity calculated as a_{w} = RH/100.

$w_{\mathrm{org},l}$ can then be calculated and used in Eq. S18 as:

$$w_{\mathrm{org},l} = \frac{m_{\mathrm{SOA},l}}{m_{\mathrm{SOA},l} + m_{\mathrm{H_2O},l}} \tag{S20}$$

In the Raoult's law method, the mole fraction of water in layer l at the particle size of D_{p} can calculated as:

$$x_{\mathrm{w},l} = \frac{RH}{100 \times K(D_{\mathrm{p}})} \tag{S21}$$

where $K(D_{\mathrm{p}})$ is the Kelvin term at particle size of D_{p}, and can be calculated in Eq. S9. $w_{\mathrm{org},l}$ can then be calculated and used in Eq. S18 as:

$$w_{\text{org},l} = \frac{(1 - x_{\text{w},l}) \times M_{SOA}}{x_{\text{w},l} \times M_{\text{w}} + (1 - x_{\text{w},l}) \times M_{\text{SOA}}} \tag{S22}$$

where M_{SOA} is the molar mass of organics (250 g mol^{-1}) for simplification. M_{w} is the molar mass of water (18 g mol^{-1}).

S8.3 Particle size effects on phase state

Influence of particle size (d_{p}) on phase transition (T_{g}) is accounted for followed by Mahant et al. (2024) as detailed in Figure S6. ΔT_{g} is the depression of glass transition temperature relative to average T_{g} of the mixture in each layer, which is then accounted for in $T_{0,l}$ and the following calculations.

$$\log_{10}(\Delta T_g) = 1.83 - 10^{(0.43 \times (\log_{10}(d_p) - 2.37))} \tag{S23}$$

$$T_{0,l} = \frac{39.17 \times (T_{\text{g},l} - \Delta T_{\text{g}})}{D + 39.17} \tag{S24}$$

S8.4 D_{b}-C^* parameterization by Kang et al. (2026)

Following Kang et al. (2026), we express the dependence of self-diffusivity of each species ($D_{\text{b,298}}$) on the effective saturation mass concentration at 298 K (C^*_{298}) in a log-log relationship.

$$\log_{10}(D_{\text{b,298}}) = 0.761 \times \log_{10}(C^*_{298}) - 14.9 \tag{S25}$$

The diffusivity in each layer ($D_{\text{b,298},l}$) is calculated with the Vignes equation (Vignes, 1966), which is a logarithmic mixing rule and weights $D_{\text{b,298}}$ of each species i by its mass fraction w in layer l ($w_{i,l}$). Non-volatile species are assumed to adopt the same $D_{\text{b,298}}$ as the species in the lowest volatility bin. To have H_2SO_4 act as plasticizer, we use a high $D_{\text{b,298}}$ of 10^{-12} cm^2 s^{-1}.

$$D_{\text{b,298},l} = \prod_i (D_{\text{b,298},i})^{w_{i,l}} \tag{S26}$$

In line with the upper limit of viscosity in Li et al. (2016), Kang et al. (2026) use a lower limit of $D_{\text{b,298},l}$ of 10^{-20} cm^2 s^{-1}. An implementation of the particle size effect is not available for the $D_{\text{b}} - C^*$ parameterization at this moment and will be the topic of future studies.

S9 Model simulations with composition-dependent diffusion coefficients

Inserting the diffusivity parameterizations described in Sect. S8 above into KM3C, we can calculate diffusivities for each particle layer as a function of chemical composition and time (Kang et al., 2026).

As detailed in Fig. S4, the model simulations following Li et al. (2020) predict glassy solid nanoparticle phase states with glass transition temperatures (T_g) well above 300 K and diffusivities smaller than 10^{-20} cm^2 s^{-1} throughout the investigated growth events in summer and spring. Plasticizer effects of water and sulfate were taken into account (Sect. S8; Koop et al., 2011; Dette and Koop, 2015), but did not alter the modeling results substantially.

The model simulations following Kang et al. (2026) in Fig. S5 predict time-dependent and radially inhomogenous semi-solid phase states with diffusivities that are initially lower in summer than in spring, and of comparable magnitude overall (10^{-20} to 10^{-18} cm^2 s^{-1}). In both scenarios, the diffusivity increases over time as the particles grow by condensation of relatively more volatile compounds (Figs. S4, S5).

To explore the potential influence of nanosize effects following Cheng et al. (2015), we combined the parameterization of Li et al. (2020) with data measured by Mahant et al. (2024) and find that glass transition temperatures decrease substantially ($\Delta T_g \sim 40 - 50$ K), but not below 300 K. As the nanoparticle size effect declines towards larger particle sizes (Fig. S6), condensation of higher volatile vapors offsets this change, leading to a near-constant T_g around 320 K. In contrast, Virtanen et al. (2010) and Virtanen et al. (2011) found an amorphous solid phase state for Finnish boreal forest aerosol particles. They reported that particle bounce decreased at the smallest diameters they investigated (17-30 nm), suggesting that these particles may not have been glassy. Thus, the relations between nanoparticle growth, phase state, and bounce as well as additional effects such as enhanced mobility in the surface layers of solid particles (quasi-liquid layers) warrant further investigation in follow-up studies (McNeill et al., 2006; Stevenson and Wolynes, 2008; Tian et al., 2022).

S10 Volatility basis sets vs. molecular resolution

Our model currently assigns identical self-diffusion coefficients to the many different organic compounds lumped into each bin of the applied decadic volatility basis sets (VBS). We note, however, that molecules in the same VBS bin may exhibit different properties such as diffusivity and desorption lifetime based on their molecular structure and functionalities, even if they exhibit similar intrinsic volatilities. Furthermore, the properties of organic aerosol mixtures may deviate from linear combinations of individual species properties. Fully resolving SOA nanoparticle growth may thus require a detailed accounting of matrix interactions, molecular identities and molecular corridors along which the gas-phase and condensed-phase composition of organic aerosols evolve (Shiraiwa et al., 2014; Li et al., 2016; Knopf et al., 2024).

Supplementary Figures

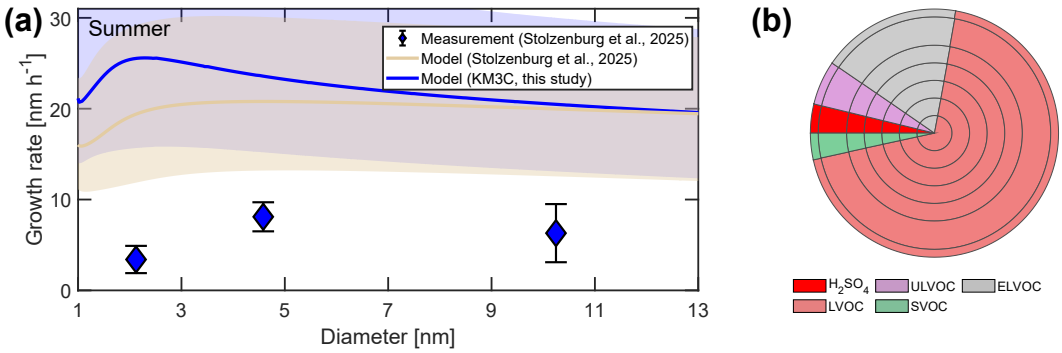

Figure S1. Observed and modelled atmospheric nanoparticle growth rates in a field experiment (Hyytiälä, 17th August, 2020). Same as Figs. 1a,c, but a higher diffusivity ($D_{\mathrm{b},298} = 10^{-15}$ cm^2 s^{-1}) is utilized in KM3C modeling. **(a)** Observed growth rates (blue diamond markers and error bars representing arithmetic mean values and standard deviations) and vapor concentration-based predictions obtained with a two-film model (Stolzenburg et al., 2025, brown line and shading for best estimate and uncertainty range by shifting full VBS by $\pm$ 1 bin). The new multiphase kinetic model (KM3C; blue line and shading for best estimate and uncertainty range by shifting full VBS by $\pm$ 1 bin) predicts similar growth rates to Stolzenburg et al. (2025) but also overestimates the observed growth rates. **(b)** Higher diffusivity ($D_{\mathrm{b},298} = 10^{-15}$ cm^2 s^{-1}) leads to well-mixed particles.

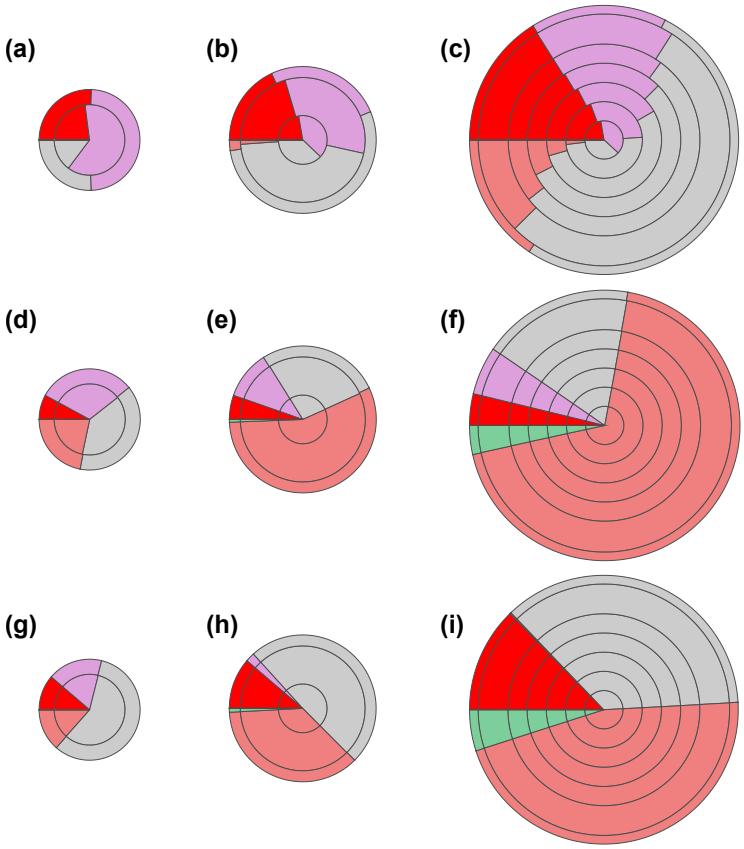

Figure S2. Radial concentration profiles for nanoparticles at diameters of 1.5 nm, 3 nm, and 7 nm for **(a-c)** the summer case with lower diffusivity ($D_{\mathrm{b},298}$ = 10^{-20} cm^2 s^{-1}), **(d-f)** the summer case with higher diffusivity ($D_{\mathrm{b},298}$ = 10^{-15} cm^2 s^{-1}) and **(g-i)** the spring case with higher diffusivity ($D_{\mathrm{b},298}$ = 10^{-15} cm^2 s^{-1}), respectively. The analysis shows that the particle core largely retains the initial composition dominated by relatively less volatile vapors (ELVOC, ULVOC) when diffusivity is low (panels a-c). In a sensitivity test with high diffusivity and otherwise unchanged conditions, relatively more volatile vapors (SVOC, LVOC) are readily taken up and well-mixed throughout the particle (panels d-f).

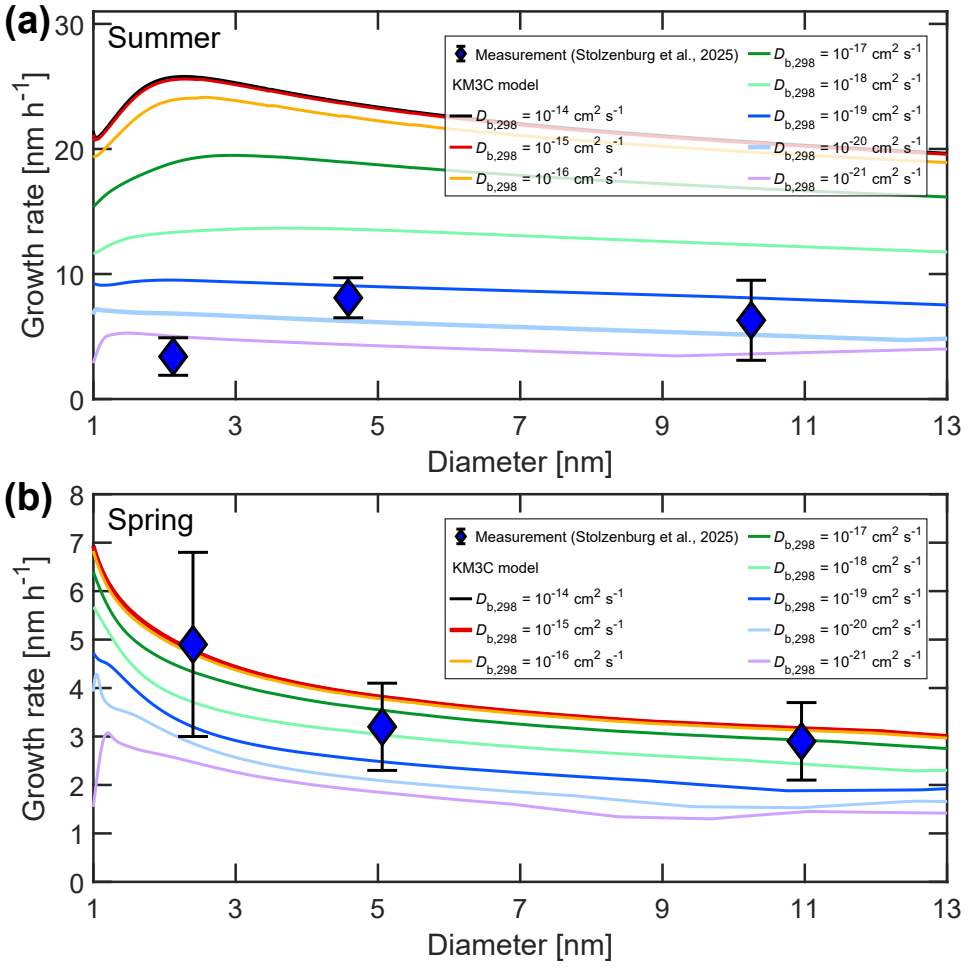

Figure S3. Observed (blue diamond markers and error bars) and KM3C-modelled (solid lines) atmospheric nanoparticle growth rates at a boreal forest site (Hyytiälä, Finland) in **(a)** summer and **(b)** spring, respectively. A range of diffusivities ($D_{b,298} = 10^{-21} - 10^{-14}$ cm^2 s^{-1}) shown with different colors is utilized in KM3C simulations.

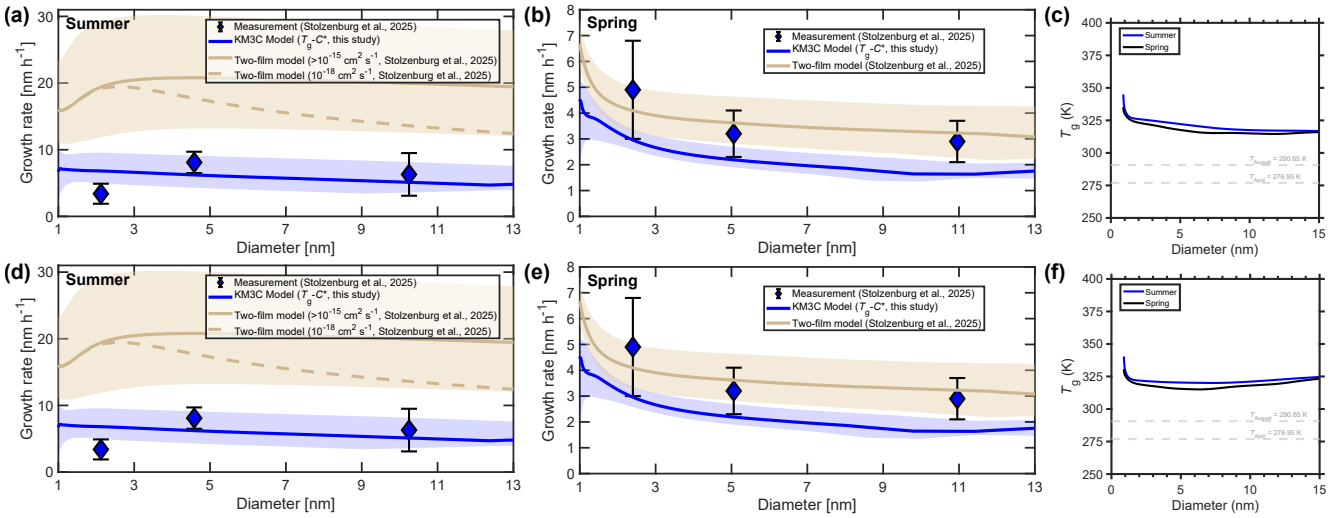

Figure S4. Observed (blue diamond markers and error bars) and modelled atmospheric nanoparticle growth rates in field experiments (Hyytiälä, Finland) in summer **(a, d)** and spring **(b, e)**, respectively. Brown line and shading represent a two-film model (Stolzenburg et al., 2025). Blue line and shading represent the KM3C model in which diffusivity is estimated following Li et al. (2020). Panels **(c)** and **(f)** show the predicted average glass transition temperature (T_g) as a function of particle size. In all the simulations shown here, T_g depression as a function of nanoparticle size following Mahant et al. (2024) is considered. In panels **(a-c)**, the water content of the SOA-H_2SO_4-water mixture is calculated using Raoult's law. In panels **(d-f)**, the water content of the mixture is calculated using an effective hygroscopicity parameter κ of approximately 0.01 as reported by Mikhailov et al. (2013) for the hygroscopic growth of ambient SOA under subsaturated conditions (RH $\sim$ 50%).

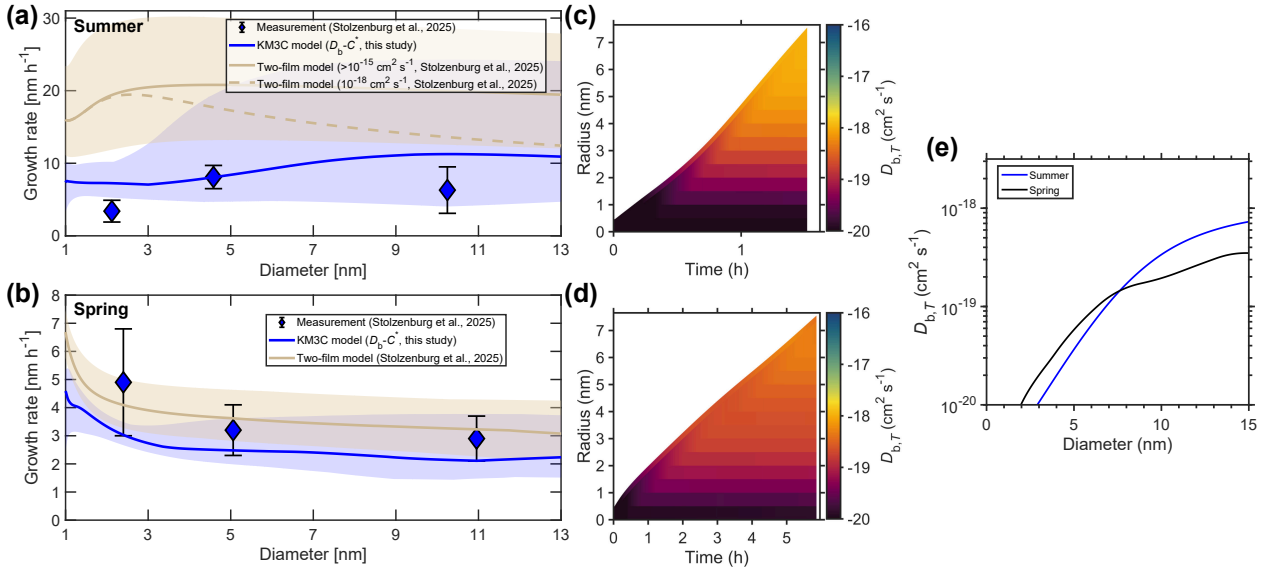

Figure S5. Observed (blue diamond markers and error bars) and modelled atmospheric nanoparticle growth rates in field experiments (Hyytiälä, Finland) in **(a)** summer and **(b)** spring, respectively. Brown line and shading represent a two-film model (Stolzenburg et al., 2025). Blue line and shading represent the KM3C model in which diffusivity is estimated following Kang et al. (2026). Panels **(c)** and **(d)** show the radial profiles of diffusivity as a function of time in summer and spring, respectively. Panel **(e)** shows the predicted diffusivity as a function of particle size using the average particle composition.

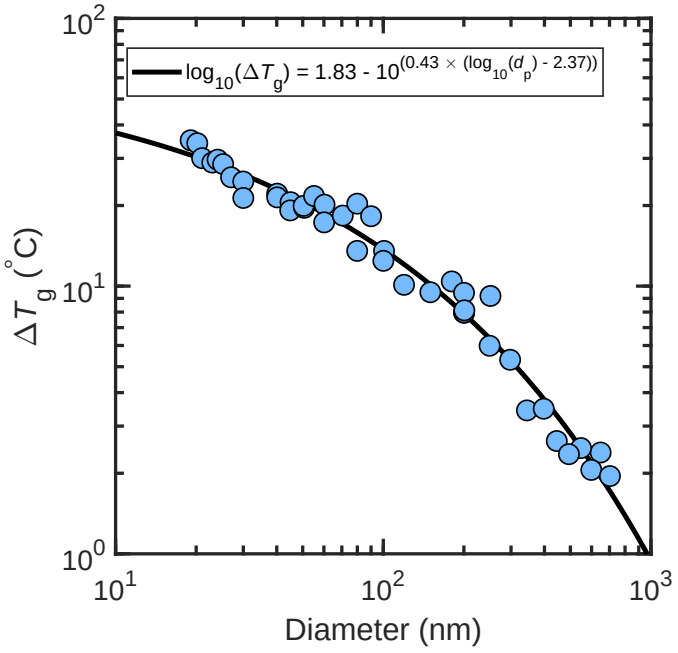

Figure S6. Glass transition temperature depression as a function of nanoparticle diameter. The black solid line represents fitting an exponential function to experimental data (blue circular markers) digitized from Mahant et al. (2024).

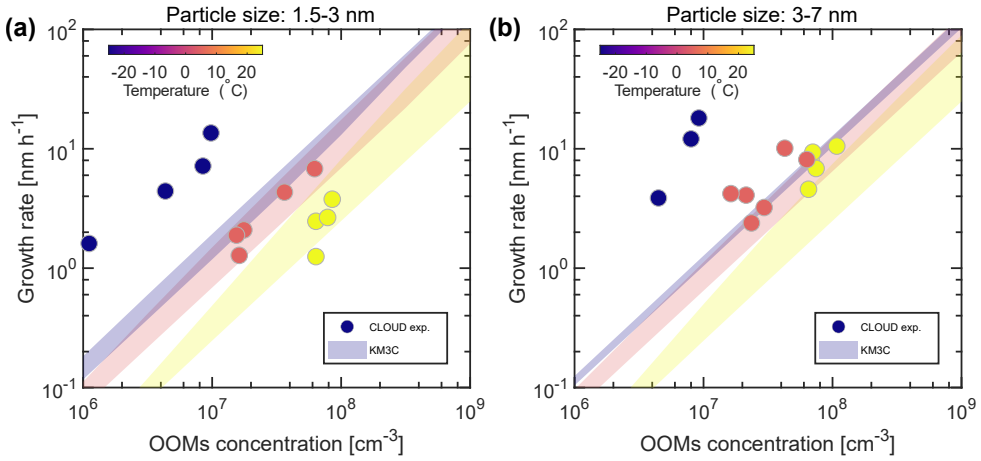

Figure S7. Nanoparticle growth rates in laboratory chamber experiments in the CERN CLOUD chamber and simulated with the KM3C kinetic model. Same as Fig. 2, but KM3C (colored bands) simulates nanoparticle growth rates for **(a)** 1.5-3 nm and **(b)** 3-7 nm using only the concentration of OOMs measured by NO3-CIMS data provided in Stolzenburg et al. (2018). Colored bands are obtained by linearly scaling the condensable organic material concentrations in the model at the three respective temperatures (-25, 5 and 25°C). Upper and lower boundaries of the shaded areas are obtained by varying the bulk diffusion coefficient $D_{b,298}$ within 10^{-20} – 10^{-15} cm^2 s^{-1} and detailed in Sect. S5.

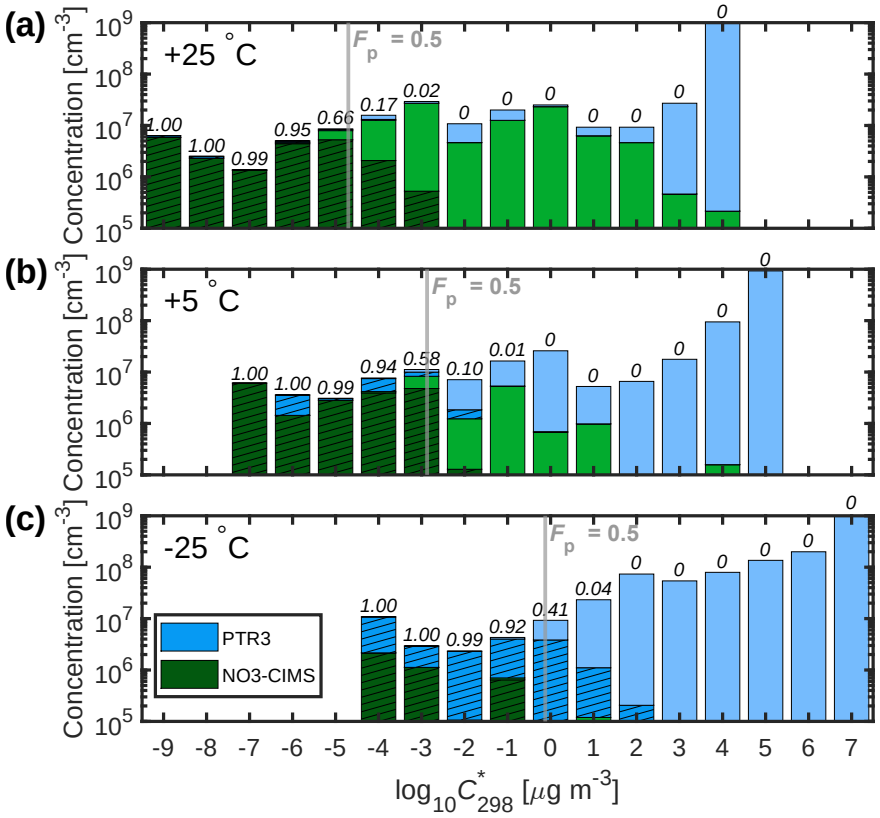

Figure S8. Volatility distributions of three experiments in the CERN CLOUD chamber. Experiments were conducted at **(a)** 25 °C, **(b)** 5 °C and **(c)** -25 °C reported by Stolzenburg et al. (2018). Data were digitized from the published Fig. 1 in Stolzenburg et al. (2018) using WebPlotDigitizer. Shaded areas and numbers above the bars indicate fractions that partition into the particle phase (F_p) at an aerosol mass loading of 2×10^{-5} µg m^{-3} assuming equilibrium partitioning in a closed system (Pankow, 1994), corresponding to 10^3 particles cm^{-3} with 3 nm diameter, and the grey vertical lines indicate the volatility where F_p = 0.5.

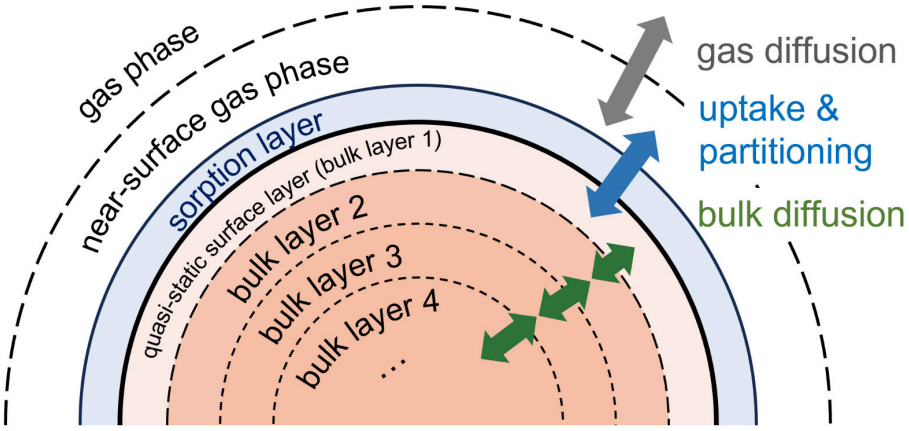

Figure S9. Overview of the kinetic multilayer model of multiphase chemistry (KM3C) used in this study. The particle bulk is subdivided into model layers to form concentration gradients and address slow diffusion.

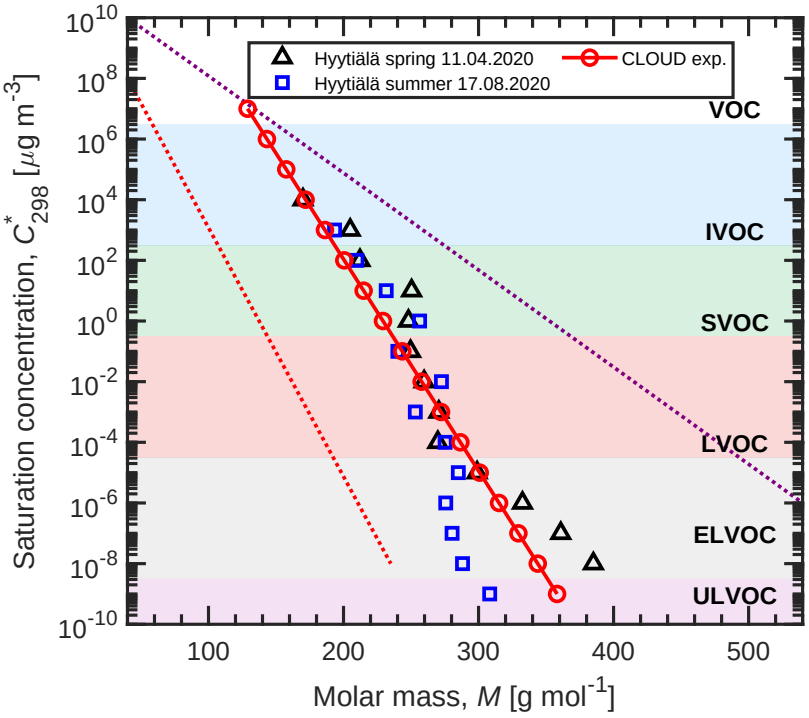

Figure S10. Molecular corridors of SOA evolution. KM3C incorporates volatility (298 K) and molar mass data from the field measurements in Hyytiälä, Finland, 11th April, 2020 (black triangles) and 17th August, 2020 (blue squares) in Stolzenburg et al. (2025). A linear relationship derived from these field measurements is applied to the CERN CLOUD chamber simulations (red circles).

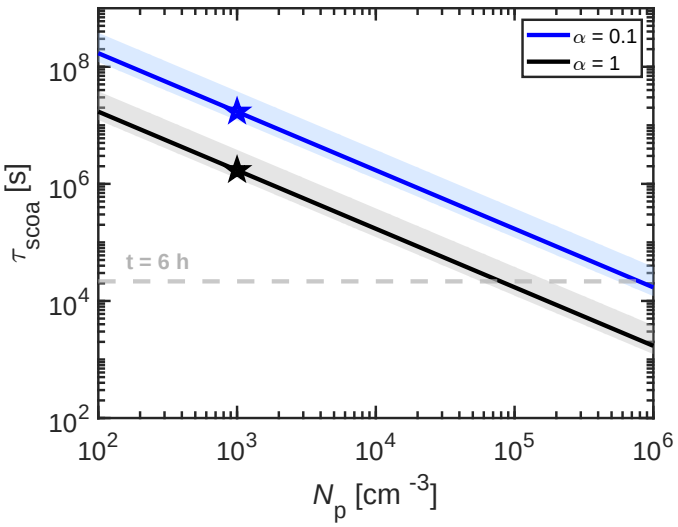

Figure S11. Characteristic self-coagulation timescale for monodisperse particles as a function of different particle number concentrations ($N_p = 10^2$ - 10^6 cm^{-3}) at 5 nm (solid lines) and for the range of 1-10 nm (shadings), where the upper bound corresponds to 1 nm and the lower bound to 10 nm. Calculations were performed for coagulation efficiencies (α) of 0.1 (blue) and 1 (black). The star-shaped markers indicate a nanoparticle concentration level of 10^3 cm^{-3} as indicated by Stolzenburg et al. (2025) (DOI: 10.48436/9633r-zf904).

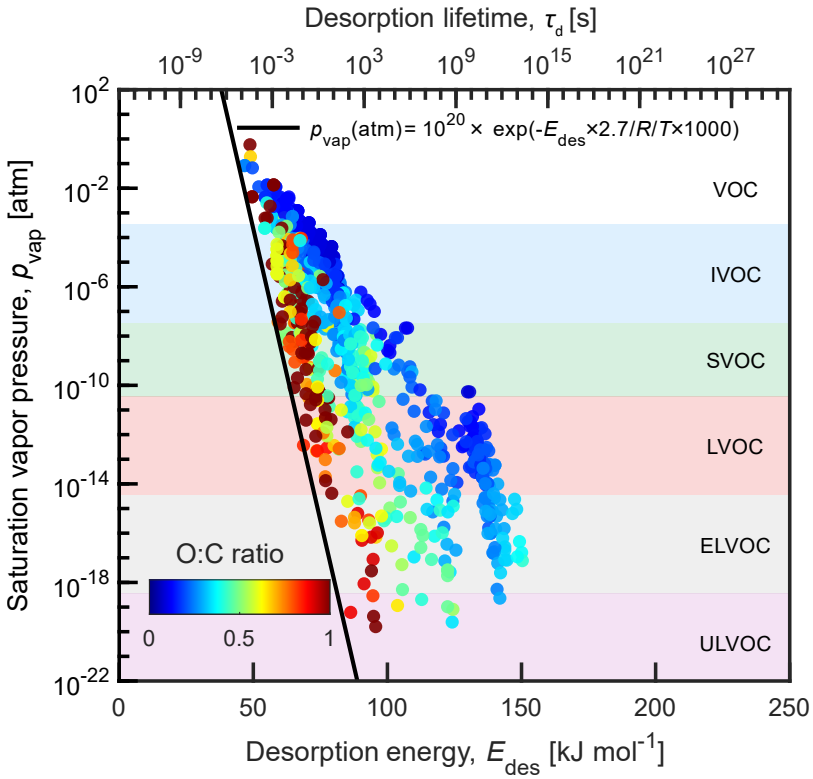

Figure S12. Relationship between saturation vapor pressure (p_{vap} at 298 K), desorption energies (E_{des}) implemented in KM3C. Desorption lifetime (τ_d) of species with a molar mass of 220 g mol^{-1} at 298 K is shown on the top axis. Markers indicate literature data (Knopf et al., 2024), where the colors show the O:C of the molecules. The black line is drawn using the shown equation, which is the parameterization used to retrieve E_{des} in KM3C.

Supplementary Tables

Table S1. Species measured in field measurements at a boreal forest site (Hyytiälä, Finland, 11 April and 17 August 2020) and in laboratory experiments (CERN CLOUD chamber), along with the volatility at 298 K and molar mass for each species used in KM3C in this study.

Species	Molar mass (Summer, g mol^{-1})	Molar mass (Spring, g mol^{-1})	Molar mass (CLOUD exp., g mol^{-1})
SOA (C^* = 10^7 µg m^{-3})	-	-	129
SOA (C^* = 10^6 µg m^{-3})	-	-	143
SOA (C^* = 10^5 µg m^{-3})	-	-	158
SOA (C^* = 10^4 µg m^{-3})	-	170	172
SOA (C^* = 10^3 µg m^{-3})	193	205	186
SOA (C^* = 10^2 µg m^{-3})	210	212	201
SOA (C^* = 10^1 µg m^{-3})	232	250	215
SOA (C^* = 10^0 µg m^{-3})	256	248	229
SOA (C^* = 10^{-1} µg m^{-3})	240	250	244
SOA (C^* = 10^{-2} µg m^{-3})	273	260	258
SOA (C^* = 10^{-3} µg m^{-3})	253	271	272
SOA (C^* = 10^{-4} µg m^{-3})	275	270	287
SOA (C^* = 10^{-5} µg m^{-3})	285	299	301
SOA (C^* = 10^{-6} µg m^{-3})	276	333	315
SOA (C^* = 10^{-7} µg m^{-3})	280	361	330
SOA (C^* = 10^{-8} µg m^{-3})	288	385	344
SOA (C^* = 10^{-9} µg m^{-3})	308	-	358
SOA (non-volatile) [a]	308	385	358
H_2SO_4 [b]	98	98	-

[a] Species in pre-existing nanoparticles are assumed to be non-volatile and are grouped into ULVOC in this study, and the molar mass of them are assumed to be the same as species in the lowest volatility bin.

[b] H_2SO_4 is assumed to have negligible vapor pressure following the assumption in the previous literature (Nieminen et al., 2010; Häkkinen et al., 2013).

Table S2. Diffusion coefficients used in this study at different temperatures for simulating nanoparticle growth in field and CERN CLOUD chamber studies.

	T (°C)	$D_{\mathrm{b},T}$ ($\mathrm{cm^2\,s^{-1}}$)		
		$D_{\mathrm{b},298} = 1 \times 10^{-15}$ ($\mathrm{cm^2\,s^{-1}}$)	$D_{\mathrm{b},298} = 1 \times 10^{-18}$ ($\mathrm{cm^2\,s^{-1}}$)	$D_{\mathrm{b},298} = 1 \times 10^{-20}$ ($\mathrm{cm^2\,s^{-1}}$)
Field	17.5 (summer)	-	6.59×10^{-19}	6.59×10^{-21}
	3.8 (spring)	2.91×10^{-16}	2.91×10^{-19}	-
CERN CLOUD chamber	-25	3.87×10^{-17}	3.87×10^{-20}	3.87×10^{-22}
	5	3.13×10^{-16}	3.13×10^{-19}	3.13×10^{-21}
	25	1×10^{-15}	1×10^{-18}	1×10^{-20}

References

Angell, C.: Relaxation in liquids, polymers and plastic crystals — strong/fragile patterns and problems, J. Non-Cryst. Solids, 131-133, 13–31, https://doi.org/https://doi.org/10.1016/0022-3093(91)90266-9, 1991.

Berkemeier, T., Takeuchi, M., Eris, G., and Ng, N. L.: Kinetic modeling of formation and evaporation of secondary organic aerosol from NO_3 oxidation of pure and mixed monoterpenes, Atmos. Chem. Phys., 20, 15 513–15 535, https://doi.org/10.5194/acp-20-15513-2020, 2020.

Bilde, M., Barsanti, K., Booth, M., Cappa, C. D., Donahue, N. M., Emanuelsson, E. U., McFiggans, G., Krieger, U. K., Marcolli, C., Topping, D., Ziemann, P., Barley, M., Clegg, S., Dennis-Smither, B., Hallquist, M., Hallquist, M., Khlystov, A., Kulmala, M., Mogensen, D., Percival, C. J., Pope, F., Reid, J. P., Ribeiro da Silva, M. A. V., Rosenoern, T., Salo, K., Soonsin, V. P., Yli-Juuti, T., Prisle, N. L., Pagels, J., Rarey, J., Zardini, A. A., and Riipinen, I.: Saturation Vapor Pressures and Transition Enthalpies of Low-Volatility Organic Molecules of Atmospheric Relevance: From Dicarboxylic Acids to Complex Mixtures, Chem. Rev., 115, 4115–4156, https://doi.org/10.1021/cr5005502, 2015.

Cai, R., Li, C., He, X.-C., Deng, C., Lu, Y., Yin, R., Yan, C., Wang, L., Jiang, J., Kulmala, M., and Kangasluoma, J.: Impacts of coagulation on the appearance time method for new particle growth rate evaluation and their corrections, Atmos. Chem. Phys., 21, 2287–2304, https://doi.org/10.5194/acp-21-2287-2021, 2021.

Cai, R., Li, X., Li, Y., Blichner, S., Stolzenburg, D., Zha, Q., Cai, J., Nie, W., Yan, C., Huang, D. D., Wang, Z., Wu, J., Yin, R., Sarnela, N., Huang, W., Tuovinen, S., Holm, S., Ahonen, L., Yao, L., Ding, A., Bianchi, F., Liu, Y., Winkler, P. M., Petäjä, T., Chen, J., Kerminen, V.-M., Wang, L., Worsnop, D., Jiang, J., Kulmala, M., and Kangasluoma, J.: The key role of nanoparticle concentration gradient in aerosol initial growth, Nat. Commun., https://doi.org/10.1038/s41467-026-70082-2, 2026.

Cappa, C. D. and Jimenez, J. L.: Quantitative estimates of the volatility of ambient organic aerosol, Atmos. Chem. Phys., 10, 5409–5424, https://doi.org/10.5194/acp-10-5409-2010, 2010.

Cheng, Y., Su, H., Koop, T., Mikhailov, E., and Pöschl, U.: Size dependence of phase transitions in aerosol nanoparticles, Nat. Commun., 6, 5923, https://doi.org/10.1038/ncomms6923, 2015.

Couvidat, F. and Sartelet, K.: The Secondary Organic Aerosol Processor (SOAP v1.0) model: a unified model with different ranges of complexity based on the molecular surrogate approach, Geosci. Model Dev., 8, 1111–1138, https://doi.org/10.5194/gmd-8-1111-2015, 2015.

Dette, H. P. and Koop, T.: Glass Formation Processes in Mixed Inorganic/Organic Aerosol Particles, J. Phys. Chem. A, 119, 4552–4561, https://doi.org/10.1021/jp5106967, 2015.

Donahue, N. M., Robinson, A. L., Stanier, C. O., and Pandis, S. N.: Coupled Partitioning, Dilution, and Chemical Aging of Semivolatile Organics, Environ. Sci. Technol., 40, 2635–2643, https://doi.org/10.1021/es052297c, 2006.

Donahue, N. M., Epstein, S. A., Pandis, S. N., and Robinson, A. L.: A two-dimensional volatility basis set: 1. organic-aerosol mixing thermodynamics, Atmos. Chem. Phys., 11, 3303–3318, https://doi.org/10.5194/acp-11-3303-2011, 2011.

Donahue, N. M., Robinson, A. L., Trump, E. R., Riipinen, I., and Kroll, J. H.: Volatility and Aging of Atmospheric Organic Aerosol, in: Atmospheric and Aerosol Chemistry, edited by McNeill, V. F. and Ariya, P. A., Topics in Current Chemistry, pp. 97–143, Springer, Berlin, Heidelberg, https://doi.org/10.1007/128_2012_355, 2014.

Donahue, N. M., Dada, L., Stolzenburg, D., Sommer, E., Simon, M., Schervish, M., DeVivo, J., Stinchfield, A., Burton, N., Bhattacharyya, N., Lopez, B., Wang, M., Scholz, W., Almeida, J., Zhao, B., Heinritzi, M., Gordon, H., Hansel, A., Curtius, J., Lehtipalo, K., El Haddad,

I., Kirkby, J., Flagan, R., Kulmala, M., and Worsnop, D.: On describing particle nucleation within the Volatility Basis Set, Atmos. Chem. Phys., 26, 8311–8339, https://doi.org/10.5194/acp-26-8311-2026, 2026.

Epstein, S. A., Riipinen, I., and Donahue, N. M.: A Semiempirical Correlation between Enthalpy of Vaporization and Saturation Concentration for Organic Aerosol, Environ. Sci. Technol., 44, 743–748, https://doi.org/10.1021/es902497z, pMID: 20025284, 2010.

Gonzalez Carracedo, L., Lehtipalo, K., Ahonen, L. R., Sarnela, N., Holm, S., Kangasluoma, J., Kulmala, M., Winkler, P. M., and Stolzenburg, D.: On the relation between apparent ion and total particle growth rates in the boreal forest and related chamber experiments, Atmos. Chem. Phys., 22, 13 153–13 166, https://doi.org/10.5194/acp-22-13153-2022, 2022.

Gordon, M. and Taylor, J. S.: Ideal copolymers and the second-order transitions of synthetic rubbers. i. non-crystalline copolymers, J. Appl. Chem., 2, 493–500, https://doi.org/10.1002/jctb.5010020901, 1952.

Häkkinen, S. A. K., Manninen, H. E., Yli-Juuti, T., Merikanto, J., Kajos, M. K., Nieminen, T., D'Andrea, S. D., Asmi, A., Pierce, J. R., Kulmala, M., and Riipinen, I.: Semi-empirical parameterization of size-dependent atmospheric nanoparticle growth in continental environments, Atmos. Chem. Phys., 13, 7665–7682, https://doi.org/10.5194/acp-13-7665-2013, 2013.

Hellén, H., Praplan, A. P., Tykkä, T., Ylivinkka, I., Vakkari, V., Bäck, J., Petäjä, T., Kulmala, M., and Hakola, H.: Long-term measurements of volatile organic compounds highlight the importance of sesquiterpenes for the atmospheric chemistry of a boreal forest, Atmos. Chem. Phys., 18, 13 839–13 863, https://doi.org/10.5194/acp-18-13839-2018, 2018.

Hou, D., Zong, D., Lindberg, C. S., Kraft, M., and You, X.: On the coagulation efficiency of carbonaceous nanoparticles, J. Aerosol Sci., 140, 105 478, https://doi.org/https://doi.org/10.1016/j.jaerosci.2019.105478, 2020.

Kang, H. G., Takeuchi, M., Ng, N. L., Pöschl, U., and Berkemeier, T.: Multiphase Chemistry and Phase State Explain Nonlinear Effects in the Formation and Evaporation of SOA from Mixed Monoterpene Precursors, ACS ES&T Air, https://doi.org/10.1021/acsestair.5c00438, 2026.

Kenseth, C. M., Hafeman, N. J., Rezgui, S. P., Chen, J., Huang, Y., Dalleska, N. F., Kjaergaard, H. G., Stoltz, B. M., Seinfeld, J. H., and Wennberg, P. O.: Particle-phase accretion forms dimer esters in pinene secondary organic aerosol, Science, 382, 787–792, https://doi.org/10.1126/science.adi0857, 2023.

Kiland, K. J., Maclean, A. M., Kamal, S., and Bertram, A. K.: Diffusion of Organic Molecules as a Function of Temperature in a Sucrose Matrix (a Proxy for Secondary Organic Aerosol), J. Phys. Chem. Lett., 10, 5902–5908, https://doi.org/10.1021/acs.jpclett.9b02182, 2019.

Kirkby, J., Curtius, J., Almeida, J., Dunne, E., Duplissy, J., Ehrhart, S., Franchin, A., Gagné, S., Ickes, L., Kürten, A., Kupc, A., Metzger, A., Riccobono, F., Rondo, L., Schobesberger, S., Tsagkogeorgas, G., Wimmer, D., Amorim, A., Bianchi, F., Breitenlechner, M., David, A., Dommen, J., Downard, A., Ehn, M., Flagan, R. C., Haider, S., Hansel, A., Hauser, D., Jud, W., Junninen, H., Kreissl, F., Kvashin, A., Laaksonen, A., Lehtipalo, K., Lima, J., Lovejoy, E. R., Makhmutov, V., Mathot, S., Mikkilä, J., Minginette, P., Mogo, S., Nieminen, T., Onnela, A., Pereira, P., Petäjä, T., Schnitzhofer, R., Seinfeld, J. H., Sipilä, M., Stozhkov, Y., Stratmann, F., Tomé, A., Vanhanen, J., Viisanen, Y., Vrtala, A., Wagner, P. E., Walther, H., Weingartner, E., Wex, H., Winkler, P. M., Carslaw, K. S., Worsnop, D. R., Baltensperger, U., and Kulmala, M.: Role of sulphuric acid, ammonia and galactic cosmic rays in atmospheric aerosol nucleation, Nature, 476, 429–433, https://doi.org/10.1038/nature10343, 2011.

Knopf, D. A., Ammann, M., Berkemeier, T., Pöschl, U., and Shiraiwa, M.: Desorption lifetimes and activation energies influencing gas–surface interactions and multiphase chemical kinetics, Atmos. Chem. Phys., 24, 3445–3528, https://doi.org/10.5194/acp-24-3445-2024, 2024.

Koop, T., Bookhold, J., Shiraiwa, M., and Pöschl, U.: Glass transition and phase state of organic compounds: dependency on molecular properties and implications for secondary organic aerosols in the atmosphere, Phys. Chem. Chem. Phys., 13, 19 238, https://doi.org/10.1039/c1cp22617g, 2011.

Kulmala, M., Kontkanen, J., Junninen, H., Lehtipalo, K., Manninen, H. E., Nieminen, T., Petäjä, T., Sipilä, M., Schobesberger, S., Rantala, P., Franchin, A., Jokinen, T., Järvinen, E., Äijälä, M., Kangasluoma, J., Hakala, J., Aalto, P. P., Paasonen, P., Mikkilä, J., Vanhanen, J., Aalto, J., Hakola, H., Makkonen, U., Ruuskanen, T., Mauldin, R. L., Duplissy, J., Vehkamäki, H., Bäck, J., Kortelainen, A., Riipinen, I., Kurtén, T., Johnston, M. V., Smith, J. N., Ehn, M., Mentel, T. F., Lehtinen, K. E. J., Laaksonen, A., Kerminen, V.-M., and Worsnop, D. R.: Direct Observations of Atmospheric Aerosol Nucleation, Science, 339, 943–946, https://doi.org/10.1126/science.1227385, 2013.

Lehtipalo, K., Leppä, J., Kontkanen, J., Kangasluoma, J., Franchin, A., Wimnner, D., Schobesberger, S., Junninen, H., Petäjä, T., Sipilä, M., Mikkilä, J., Vanhanen, J., Worsnop, D., and Kulmala, M.: Methods for determining particle size distribution and growth rates between 1 and 3 nm using the Particle Size Magnifier, Boreal Environ. Res., 19, 215–236, 2014.

Li, Y., Pöschl, U., and Shiraiwa, M.: Molecular corridors and parameterizations of volatility in the chemical evolution of organic aerosols, Atmos. Chem. Phys., 16, 3327–3344, https://doi.org/10.5194/acp-16-3327-2016, 2016.

Li, Y., Day, D. A., Stark, H., Jimenez, J. L., and Shiraiwa, M.: Predictions of the glass transition temperature and viscosity of organic aerosols from volatility distributions, Atmos. Chem. Phys., 20, 8103–8122, https://doi.org/10.5194/acp-20-8103-2020, 2020.

Maben, H. K. and Ziemann, P. J.: Kinetics of oligomer-forming reactions involving the major functional groups present in atmospheric secondary organic aerosol particles, Environ. Sci.: Processes Impacts, 25, 214–228, https://doi.org/10.1039/D2EM00124A, 2023.

Mahant, S., Snider, J. R., Petters, S. S., and Petters, M. D.: Effect of Aerosol Size on Glass Transition Temperature, J. Phys. Chem. Lett., 15, 7509–7515, https://doi.org/10.1021/acs.jpclett.4c01415, 2024.

McNeill, V. F., Loerting, T., Geiger, F. M., Trout, B. L., and Molina, M. J.: Hydrogen chloride-induced surface disordering on ice, P. Natl. Acad. Sci. USA, 103, 9422–9427, https://doi.org/10.1073/pnas.0603494103, 2006.

Mehra, A., Krechmer, J. E., Lambe, A., Sarkar, C., Williams, L., Khalaj, F., Guenther, A., Jayne, J., Coe, H., Worsnop, D., Faiola, C., and Canagaratna, M.: Oligomer and highly oxygenated organic molecule formation from oxidation of oxygenated monoterpenes emitted by California sage plants, Atmos. Chem. Phys., 20, 10 953–10 965, https://doi.org/10.5194/acp-20-10953-2020, 2020.

Mikhailov, E., Vlasenko, S., Rose, D., and Pöschl, U.: Mass-based hygroscopicity parameter interaction model and measurement of atmospheric aerosol water uptake, Atmos. Chem. Phys., 13, 717–740, https://doi.org/10.5194/acp-13-717-2013, 2013.

Mishra, A., Kilchhofer, K., Iezzi, L., Pöschl, U., Alpert, P. A., Ammann, M., and Berkemeier, T.: Photochemical Degradation of Iron Citrate in Anoxic Viscous Films Enhanced by Redox Cascades, ACS Earth Space Chem., 9, 689–698, https://doi.org/10.1021/acsearthspacechem.4c00364, 2025.

Nguyen, K., Schervish, M., Lakey, P. S. J., Smith, J. N., and Shiraiwa, M.: Impact of particle phase state on the competition between condensation and coagulation, Environ. Sci.: Atmos., 6, 152–165, https://doi.org/10.1039/d5ea00069f, 2026.

Nieminen, T., Lehtinen, K. E. J., and Kulmala, M.: Sub-10 nm particle growth by vapor condensation – effects of vapor molecule size and particle thermal speed, Atmos. Chem. Phys., 10, 9773–9779, https://doi.org/10.5194/acp-10-9773-2010, 2010.

Pankow, J. F.: An absorption model of the gas/aerosol partitioning involved in the formation of secondary organic aerosol, Atmos. Environ., 28, 189–193, https://doi.org/10.1016/1352-2310(94)90094-9, 1994.

Petters, M. D. and Kreidenweis, S. M.: A single parameter representation of hygroscopic growth and cloud condensation nucleus activity, Atmos. Chem. Phys., 7, 1961–1971, https://doi.org/10.5194/acp-7-1961-2007, 2007.

Pöschl, U., Rudich, Y., and Ammann, M.: Kinetic model framework for aerosol and cloud surface chemistry and gas-particle interactions ndash; Part 1: General equations, parameters, and terminology, Atmos. Chem. Phys., 7, 5989–6023, https://doi.org/10.5194/acp-7-5989-2007, 2007.

Schervish, M. and Donahue, N. M.: Peroxy radical chemistry and the volatility basis set, Atmos. Chem. Phys., 20, 1183–1199, https://doi.org/10.5194/acp-20-1183-2020, 2020.

Seinfeld, J. H. and Pandis, S. N.: Atmospheric chemistry and physics: from air pollution to climate change, John Wiley & Sons, 2016.

Shiraiwa, M., Pfrang, C., Koop, T., and Pöschl, U.: Kinetic multi-layer model of gas-particle interactions in aerosols and clouds (KM-GAP): linking condensation, evaporation and chemical reactions of organics, oxidants and water, Atmos. Chem. Phys., 12, 2777–2794, https://doi.org/10.5194/acp-12-2777-2012, 2012.

Shiraiwa, M., Berkemeier, T., Schilling-Fahnestock, K. A., Seinfeld, J. H., and Pöschl, U.: Molecular corridors and kinetic regimes in the multiphase chemical evolution of secondary organic aerosol, Atmos. Chem. Phys., 14, 8323–8341, https://doi.org/10.5194/acp-14-8323-2014, 2014.

Shiraiwa, M., Li, Y., Tsimpidi, A. P., Karydis, V. A., Berkemeier, T., Pandis, S. N., Lelieveld, J., Koop, T., and Pöschl, U.: Global distribution of particle phase state in atmospheric secondary organic aerosols, Nat. Commun., 8, 15 002, https://doi.org/10.1038/ncomms15002, 2017.

Stevenson, J. D. and Wolynes, P. G.: On the surface of glasses, J. Chem. Phys., 129, 234 514, https://doi.org/10.1063/1.3041651, 2008.

Stolzenburg, D., Fischer, L., Vogel, A. L., Heinritzi, M., Schervish, M., Simon, M., Wagner, A. C., Dada, L., Ahonen, L. R., Amorim, A., Baccarini, A., Bauer, P. S., Baumgartner, B., Bergen, A., Bianchi, F., Breitenlechner, M., Brilke, S., Buenrostro Mazon, S., Chen, D., Dias, A., Draper, D. C., Duplissy, J., El Haddad, I., Finkenzeller, H., Frege, C., Fuchs, C., Garmash, O., Gordon, H., He, X., Helm, J., Hofbauer, V., Hoyle, C. R., Kim, C., Kirkby, J., Kontkanen, J., Kürten, A., Lampilahti, J., Lawler, M., Lehtipalo, K., Leiminger, M., Mai, H., Mathot, S., Mentler, B., Molteni, U., Nie, W., Nieminen, T., Nowak, J. B., Ojdanic, A., Onnela, A., Passananti, M., Petäjä, T., Quéléver, L. L. J., Rissanen, M. P., Sarnela, N., Schallhart, S., Tauber, C., Tomé, A., Wagner, R., Wang, M., Weitz, L., Wimmer, D., Xiao, M., Yan, C., Ye, P., Zha, Q., Baltensperger, U., Curtius, J., Dommen, J., Flagan, R. C., Kulmala, M., Smith, J. N., Worsnop, D. R., Hansel, A., Donahue, N. M., and Winkler, P. M.: Rapid growth of organic aerosol nanoparticles over a wide tropospheric temperature range, P. Natl. Acad. Sci. USA, 115, 9122–9127, https://doi.org/10.1073/pnas.1807604115, 2018.

Stolzenburg, D., Wang, M., Schervish, M., and Donahue, N. M.: Tutorial: Dynamic organic growth modeling with a volatility basis set, J. Aerosol Sci., 166, 106 063, https://doi.org/10.1016/j.jaerosci.2022.106063, 2022.

Stolzenburg, D., Cai, R., Blichner, S. M., Kontkanen, J., Zhou, P., Makkonen, R., Kerminen, V.-M., Kulmala, M., Riipinen, I., and Kangasluoma, J.: Atmospheric nanoparticle growth, Rev. Mod. Phys., 95, 045 002, https://doi.org/10.1103/RevModPhys.95.045002, 2023.

Stolzenburg, D., Sarnela, N., Bianchi, F., Cai, J., Cai, R., Cheng, Y., Dada, L., Donahue, N. M., Grothe, H., Holm, S., Kerminen, V.-M., Lehtipalo, K., Petäjä, T., Sulo, J., Winkler, P. M., Yan, C., Kangasluoma, J., and Kulmala, M.: Incomplete mass closure in atmospheric nanoparticle growth, npj Clim. Atmos. Sci., 8, https://doi.org/10.1038/s41612-025-00893-5, 2025.

Tian, H., Xu, Q., Zhang, H., Priestley, R. D., and Zuo, B.: Surface dynamics of glasses, Appl. Phys. Rev., 9, 011 316, https://doi.org/10.1063/5.0083726, 2022.

Tröstl, J., Chuang, W. K., Gordon, H., Heinritzi, M., Yan, C., Molteni, U., Ahlm, L., Frege, C., Bianchi, F., Wagner, R., Simon, M., Lehtipalo, K., Williamson, C., Craven, J. S., Duplissy, J., Adamov, A., Almeida, J., Bernhammer, A.-K., Breitenlechner, M., Brilke, S., Dias, A., Ehrhart, S., Flagan, R. C., Franchin, A., Fuchs, C., Guida, R., Gysel, M., Hansel, A., Hoyle, C. R., Jokinen, T., Junninen, H., Kangasluoma, J., Keskinen, H., Kim, J., Krapf, M., Kürten, A., Laaksonen, A., Lawler, M., Leiminger, M., Mathot, S., Möhler, O., Nieminen, T., Onnela, A., Petäjä, T., Piel, F. M., Miettinen, P., Rissanen, M. P., Rondo, L., Sarnela, N., Schobesberger, S., Sengupta, K., Sipilä, M., Smith,

J. N., Steiner, G., Tomè, A., Virtanen, A., Wagner, A. C., Weingartner, E., Wimmer, D., Winkler, P. M., Ye, P., Carslaw, K. S., Curtius, J., Dommen, J., Kirkby, J., Kulmala, M., Riipinen, I., Worsnop, D. R., Donahue, N. M., and Baltensperger, U.: The role of low-volatility organic compounds in initial particle growth in the atmosphere, Nature, 533, 527–531, https://doi.org/10.1038/nature18271, 2016.

Vignes, A.: Diffusion in Binary Solutions. Variation of Diffusion Coefficient with Composition, Ind. Eng. Chem. Fundam., 5, 189–199, https://doi.org/10.1021/i160018a007, 1966.

Virtanen, A., Joutsensaari, J., Koop, T., Kannosto, J., Yli-Pirilä, P., Leskinen, J., Mäkelä, J. M., Holopainen, J. K., Pöschl, U., Kulmala, M., Worsnop, D. R., and Laaksonen, A.: An amorphous solid state of biogenic secondary organic aerosol particles, Nature, 467, 824–827, https://doi.org/10.1038/nature09455, 2010.

Virtanen, A., Kannosto, J., Kuuluvainen, H., Arffman, A., Joutsensaari, J., Saukko, E., Hao, L., Yli-Pirilä, P., Tiitta, P., Holopainen, J. K., Keskinen, J., Worsnop, D. R., Smith, J. N., and Laaksonen, A.: Bounce behavior of freshly nucleated biogenic secondary organic aerosol particles, Atmos. Chem. Phys., 11, 8759–8766, https://doi.org/10.5194/acp-11-8759-2011, 2011.